magnetism

MDPI

Article

Influence of Hydrogen Reduction Stage Conditions on the Microwave Properties of Fine Iron Powders Obtained via a Spray-Pyrolysis Technique

Anastasia V. Artemova *, Sergey S. Maklakov, Artem O. Shiryaev, Alexey V. Osipov, Dmitry A. Petrov, Konstantin N. Rozanov and Andrey N. Lagarkov

Institute for Theoretical and Applied Electromagnetics RAS, Moscow 125412, Russia; squirrel498@gmail.com (S.S.M.); artemshiryaev@mail.ru (A.O.S.); avosipov@mail.ru (A.V.O.); dpetrov-itae@yandex.ru (D.A.P.); k.rozanov@yandex.ru (K.N.R.); maklakov@itae.ru (A.N.L.)
* Correspondence: avometras@gmail.com

Abstract: The relationship between the chemical purity of one-size particles and microwave properties in ferromagnetic materials is not clearly studied. Ferromagnetic nanostructured iron powders were synthesized from iron nitrate solution using ultrasonic spray-pyrolysis and then reduced in H_2 flow at 350, 400, 450, and 500 °C. A rise in the concentration of solutions of a precursor from 10 to 20 wt. % led to an increase in mean particle size. The interrelationship was studied between chemical composition and the microwave dispersion of the powders obtained. An increase in the temperature of reduction changes the chemical composition and increases the amplitude of complex microwave permeability, which was studied using solid-state physics methods (XRD, STA, SEM, and VNA). It was found that annealing at 400 °C is the optimal treatment that allows the production of iron powders, consisting of about 90% of α-Fe phase, possessing a particle surface with low roughness and porosity, and demonstrating intense microwave absorption. Annealing at a higher temperature (500 °C) causes an even higher increase in permeability but leads to the destruction of nanostructured spheres into smaller particles due to grain growth. This destruction causes an abrupt increase in permittivity and therefore significantly reduces potential applications of the product. The insight into chemical–magnetic relationships of these materials enhances the data for design applications in magnetic field sensing.

Keywords: spray-pyrolysis; magnetic properties; microwave permeability; chemical composition

check for updates

Citation: Artemova, A.V.; Maklakov, S.S.; Shiryaev, A.O.; Osipov, A.V.; Petrov, D.A.; Rozanov, K.N.; Lagarkov, A.N. Influence of Hydrogen Reduction Stage Conditions on the Microwave Properties of Fine Iron Powders Obtained via a Spray-Pyrolysis Technique. *Magnetism* **2023**, *3*, 90–101. https://doi.org/10.3390/magnetism3020008

Academic Editors: Manish Kumar, Sanjay Kumar Upadhyay and Jitendra Pal Singh

Received: 20 March 2023
Revised: 11 April 2023
Accepted: 19 April 2023
Published: 23 April 2023

1. Introduction

The features of the complex microwave permeability $\mu' + i{\cdot}\mu''$ and permittivity $\varepsilon' + i{\cdot}\varepsilon''$ of composites filled with magnetic powders depend on structure–property relationships between structure elements and on the chemical state of the components. In the first case, the filler particle's shape (spheres, discs, flakes, etc.), the matrix–inclusion interface, agglomeration, and dispersion of inclusions in the matrix govern these properties. These phenomena underlie a classical understanding of the propagation of electromagnetic waves in a medium [1,2]. According to effective medium theory (e.g., the Maxwell–Garnett equation [3]), an increase in the inclusion content in the composites leads to the growth of the absorption properties. This was demonstrated elsewhere, e.g., by using carbonyl iron powder [4] and ferrite [5]. In the second case—the chemical composition and the presence of impurities in materials—the crystalline and magnetic structure of inclusions influences both static and dynamic magnetic properties [2,6].

A few studies have reported a controlled change in the microwave properties of materials, using the principle of changing the chemical composition. For example, in soft nickel ferrites, the non-magnetic α-Fe_2O_3 phase simultaneously reduces saturation magnetization and improves frequency stability (decreases frequency dispersion) permeability [7].

Similarly, the saturation magnetization decrease has been observed with an increase in cobalt content [8] in cobalt ferrites. A change in Ti concentration in M-type hexagonal ferrite composites results in a low-frequency shift of the natural ferrimagnetic resonance frequency [9]. In ferromagnetic films, even grain growth, caused by an increase in oxygen concentration during reactive sputtering of permalloy films [10] as well as post-production annealing [11], can increase both static and dynamic magnetic properties due to a change in chemical and magnetic structure. Therefore, a consideration of the dependencies of microwave properties as a function of the chemical composition of compounds can be carried out while keeping other structural features (morphology, structure, and size) unchanged [12]. However, for metal ferromagnets, insight into the complex relationships between the parameters of microwave permeability and chemical phenomena, including chemical purity, remains unexplored, and requires further research.

The ultrasonic spray-pyrolysis technique allows for the solid spherical particles to be produced from liquid solutions with a dissolved metal component. A typical diagram of the spray-pyrolysis apparatus can be found elsewhere [13]. The principle of the process includes (i) aerosol formation from the initial solution, (ii) solvent evaporation from aerosol droplets with diffusion and crystallization of dissolved solids near the surface, and (iii) collection of the formed solid particles [14,15]. The characteristics of the final product depend on synthesis parameters, e.g., atomization frequency, solution concentration, temperature, flow rate, etc. The ability to produce particles in a wide range of chemical compositions, which possess complex structures (specifically, hollow spheres, which are of special interest for microwave applications), exotic morphology, and that are of a monodispersed size of up to microns in diameter, are advantages of this method. The transformation of oxide into pure metal during spray-pyrolysis may be carried out through the addition of reducing agents such as ethanol, ethylene glycol, and formic acid in starting solution [16]. Additionally, hydrogen can be directly inducted either into the reactor [15] or to post-anneal the as-prepared metal oxide. The temperature of reduction with H_2 in the post-annealing process is usually at around 500 °C and lower. For nanoscale oxides NiO [17], Fe_2O_3 [17], and Co_3O_4 [18], the metal reduction occurs at temperatures as low as 420 °C, 600 °C, and 500 °C, respectively. Annealing in a hydrogen flow makes it possible to finely control the reduction degree, i.e., composition, of the final product.

In previous research [19,20], hollow iron particles were synthesized by the spray-pyrolysis process using an ultrasonic atomizer with an operating frequency of 1.8 MHz and annealed at 450 °C in H_2 constant flow. It was shown that the increase in the concentration of the initial solution led to an increase in the mean size of particles from 0.6 to 1 μm and causes changes in microwave dispersion.

In the present study, the nanostructured spherical iron particles were successively synthesized by ultrasonic spray-pyrolysis and then reduced in hydrogen at 350–500 °C temperature range. The obtained powders, reduced at a different temperature, possessed invariant size and shape but differed in chemical purity. Here, it was observed that the reduction temperature influences directly the chemical composition and purity of iron powders, morphology, and their physical properties, specifically microwave permittivity. Experimental measurements of microwave permeability clearly showed the dependence of this parameter on the chemical impurity of α-Fe, keeping particle size intact. Understanding the described interrelationship presents new possibilities for the production and design of materials with desired microwave properties, especially for electromagnetic compatibility solutions and magnetic field sensing.

2. Materials and Methods

2.1. Hematite Powder Preparation Using an Ultrasonic Spray-Pyrolysis

Aerosol particles in the form of fine droplets were produced through the atomization of iron (III) nitrate nonahydrate $Fe(NO_3)_3 \cdot 9H_2O$ (≥98%, Sigma Aldrich) water solution in ultrasonic nebulizer Albedo IN-8 (Albedo, Russia). The ultrasonic piezoelectric radiator with an operating frequency of 2.64 MHz allowed for the fabrication of aerosol droplets

from prepared precursor aqueous solutions with concentrations 10 (0.5 M) and 20 wt. % (1 M) with a diameter from 0.5 to 5 µm. Aerosol particles passed through the 1000 °C heated zone of tube furnace LF-50/500-1200 (LOIP, Russia) in a quartz tube reactor (ϕ 45 mm, 100 cm in length). The flow rate of the carrier gas (air, 5 l·min^{-1}) was achieved by an oil vacuum pump through the reactor, including a cancellated filter (metal mesh, 10 µm aperture) and a system of three gas bubblers filled with water, which were used to decrease the flow and collect waste that overpasses the filter.

Therefore, starting from iron (III) nitrate precursor solution (hereafter identified as 10 and 20 sol. %) two powders of iron oxide Fe_2O_3 were collected on the filter. The product yield was approximately 1 g per hour.

2.2. Iron Powder Preparation by the Hematite Reduction in Hydrogen

The iron powders were obtained from the hematite powder. The hematite red powders (10, 20 sol. %) spread into a quartz crucible were annealed at 350, 400, 450, and 500 °C for 75 min in hydrogen flow. This gave eight black iron powders in total. Hydrogen was synthesized using hydrogen gas generator GV-12 (Meta-Chrom, Russia) with a productiveness of 12 l·min^{-1}. Before starting heating and after annealing, the reactor was blown off by high-purity inert argon gas for cleaning from atmospheric air and passivation of the surface of the powder during cooling to room temperature forming a protective oxide film [21].

2.3. Characterization

The structure and chemical phase composition of synthesized iron powders was studied by dint of a Difray 401 diffractometer (Scientific Instruments, Russia) at room temperature. The X-ray powder diffraction method (XRD) was applied for the measurements from 14° to 140° 2θ degrees using Bragg–Brentano geometry and chromium radiation (2.2901 Å). XRD results were compared with the powder diffraction file (PDF) database. The quantitative phase analysis and the average size of the crystallites were evaluated by the reference intensity ratio (RIR) method and the Scherrer formula, respectively.

Scanning electron microscopy (SEM) was performed using a LEO EVO-50 XVP (Carl Zeiss, Jena, Germany) microscope. The particle size distribution of the eight studied samples was examined manually from the SEM images, measuring approximately 500 individual particles for each powder.

The simultaneous thermal analysis (STA) instrument Netzsch STA 449 F3 Jupiter (Netzsch, Germany) was used to carry out the oxidation experiments [22]. The weight of iron powders taken for analysis was controlled at 10–20 mg to decrease the influence of the temperature gradient in the sample. Lower weightings give lower-quality STA curves, and higher weightings show problems with nonuniform heating. Simultaneous thermogravimetry (TG) and differential scanning calorimetry (DSC) measurements were performed in a corundum crucible under atmospheric pressure conditions in the temperature range from 30 to 1000 °C with a heating rate of 10 °C·min^{-1}. Dry air was used as an oxidant.

The composite samples for the microwave measurements were prepared by mixing molten paraffin wax matrix with prepared iron powders [23,24]. S-parameters of toroidal composite samples with filler fraction 75 wt. % in all cases were measured with a standard 7/3 mm coaxial line using a vector network analyzer (VNA) N5224B (Keysight, Santa Rosa, CA, USA). The measurement ports were calibrated using the TRL calibration method. The frequency dependencies of complex microwave permeability and permittivity were determined by the Nicolson–Ross–Weir [3,25] technique in the frequency range of 0.1 to 30 GHz.

The measured permeability was fitted by two Lorentzian curves [26], from which the amplitudes and resonance frequencies were found. To calculate Acher's parameter, a mass fraction of 75 % was recalculated into 25 vol. % (using the tabular density of pure iron, 7.88 g/cm^3), which was the effective volume fraction of the metal, but not the volume fraction of inclusions. The fitted frequency dispersion of microwave permeability was applied for the calculation of the Acher's parameter, i.e., a quantitative magnetic

characteristic of the composition of the material [27,28], following the formula given in [20]. Sharp peaks observed in the high-frequency region of the complex microwave permittivity are attributed to higher-order modes and not related to intrinsic material parameters of the composites [29].

3. Results and Discussion

3.1. X-ray Diffraction Analysis

X-ray diffraction analysis of the iron powders indicated the presence of high-intensity peaks of body-centered cubic (bcc) α-Fe and hexagonal α-Fe_2O_3. Figure 1 shows XRD peaks of Fe 10 sol. % and 20 sol. % samples reduced from iron oxide to iron in hydrogen at 350, 400, 450, and 500 °C. According to the PDF-60696 card, the tabular value of the lattice constant of the pure iron phase is 2.866 Å and the position of peaks are 68.78° (110) and 106.03° (200) 2θ. Characteristics of the iron phase coincide well with described tabular values (*vide* Table 1). For the appraisal of the lattice parameters of the hexagonal crystal system, a minimum of two peaks is required. Due to the lower intensity of peaks, located at 54.04° and 101.35° 2θ, the lattice parameters of α-Fe_2O_3 were estimated only for a few samples, close in value to a = 5.04 Å and c = 13.77 Å, which corresponds to the tabular value [30].

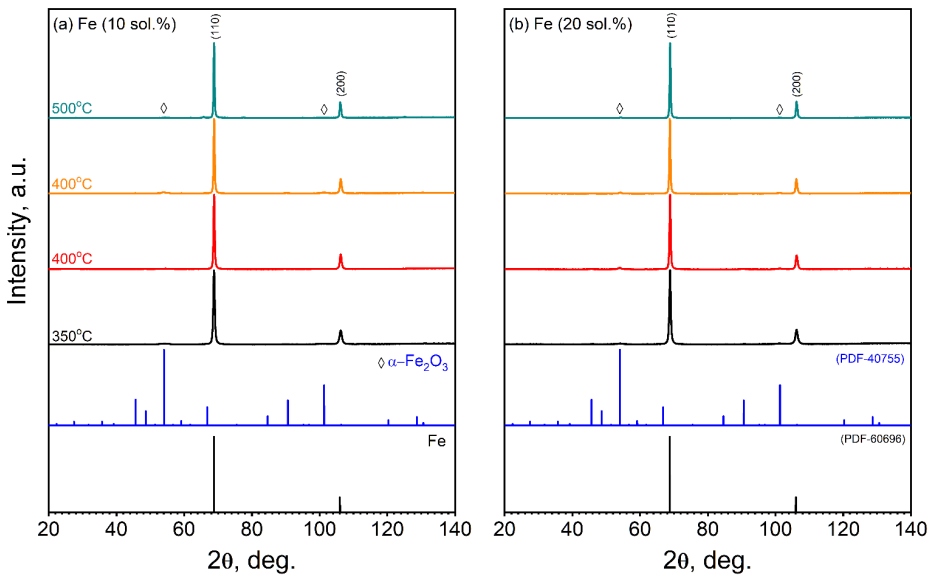

Figure 1. The X-ray diffraction patterns of Fe (**a**) 10 sol % and (**b**) 20 sol. % samples reduced from hematite to iron in hydrogen at 350–500 °C. The intensities and position of angles 2θ of samples are given in comparison with standard PDF cards of Fe and Fe_2O_3.

Table 1. XRD data and the size of iron powders produced with different temperatures of reduction T_{red}, where a—lattice constant, CS— crystallite size, ω—an evaluated mass fraction of α-Fe and α-Fe_2O_3 in each sample, d_{av}—average diameter of powder particles.

Sample	T_{red}, °C	a, Å	ω, wt. %		CS, nm		d_{av}, μm
			Fe	Fe_2O_3	Fe	Fe_2O_3	
Fe (10 sol. %)	350	2.8660	85	15	27	4	0.41
	400	2.8659 (8)	90	10	37	4	0.50
	450	2.8655 (7)	85	15	39	8	0.57
	500	2.8672 (3)	95	5	49	19	<<0.41
Fe (20 sol. %)	350	2.8656 (7)	90	10	27	6	0.69
	400	2.8649 (8)	90	10	36	10	0.70
	450	2.8664 (9)	90	10	41	12	0.78
	500	2.8647 (5)	95	5	49	17	0.80

The X-ray diffraction technique provides average structure information (degree of crystallinity, phase identification, lattice parameter) [31], but no account is taken of the particle's morphology, i.e., grains of particles or porosity. The crystallite sizes were estimated from the full width at half maximum (FWHM) of the diffraction profile. For Fe 10 sol. % and 20 sol. %, the sample crystallite size of the α-Fe phase increased from 27 to 49 nm with the increase in reduction temperature.

Semi-quantitative phase analysis was estimated using the reference intensity method. The method is based on scale factor differences between reference and measured peaks. The reference standard of corundum values for phases α-Fe (I/I_c = 10.77) and α-Fe_2O_3 (I/I_c = 4) were used. The reduction degree increased from 85 to 95 wt. % when the temperature of reduction increased from 350 to 500 °C.

The estimation of containing phase ω and crystallite size is provided in Table 1. Crystallite size and purity of iron powders increased proportionally to the reduction temperature for both samples (Fe 10 and 20 sol. %). Hydrogen content in the gas mixture, the rate and temperature of reduction, and a smaller size of powder, i.e., a larger specific area, influenced the reduction degree [32]. The Fe/Fe_2O_3 ratio was more efficiently reduced at the high-temperature reduction (500 °C), than at 350 °C.

3.2. Scanning Electron Microscopy

The SEM microphotographs showed that the increase in temperature of reduction did not change the overall particle size but resulted in the increase of porosity (see Figure 2b–d,f–h). The iron powders demonstrated a spherical nanostructured shape, consisting of agglomerated grains of iron, which is typical for particles obtained using the spray-pyrolysis technique [14].

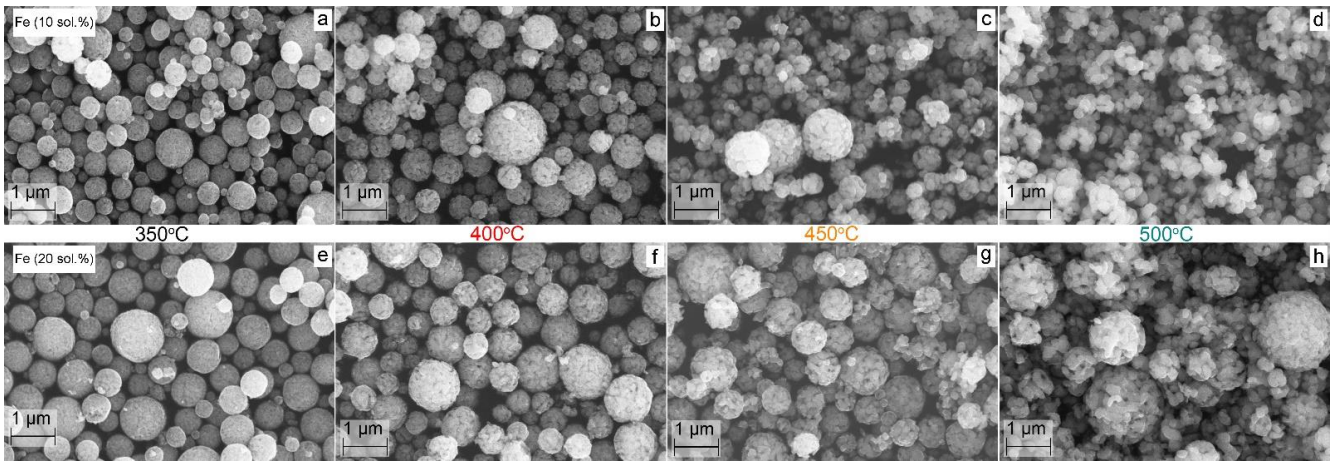

Figure 2. SEM images of the (**a**–**d**) Fe 10 sol. % and (**e**–**h**) 20 sol. % particles produced at different temperatures of reduction 350, 400, 450, and 500 °C.

Enlargement of the agglomerated grains as well as pore size with the temperature of reduction were observed. The reduction process caused grain sintering, enlargement of pores between grains [33], and rise of crystallite size (see Table 1). Pore formation can probably be explained as follows. Reduction of iron (III) oxide to iron occurs with losses in mass and volume of the sample. Straight calculation following the $2Fe_2O_3 = 4Fe + 3O_2$ reaction gives a mass loss of 42.97%. According to [34], the loss in volume during the process is ~30%. A simultaneous increase in crystallite and grain size of iron with an increase in temperature results in the formation of the observed "mesh" structure. Smooth particles can be obtained with the direct addition of hydrogen during synthesis [15]. A similar structure has previously been reported for Co [35] but has never been seen before in iron powders.

The reduction at 350 °C provided iron particles with a slick, low-roughness surface (Figure 2a,e). At higher temperatures, pores became coarser and larger. Distinct grain structure and porosity were observed at 400–500 °C temperature of reduction. Between these samples (400–500 °C), minimal grain size and porosity as well as crystallite size (37 nm) and a high mass fraction (~90%) were demonstrated in both samples after reducing at 400 °C (Figure 2b,f). This notable characteristic indicates that reducing at 400 °C provided powder with good properties, including morphology and chemical composition.

The concentration of precursor solution influenced the mean size of the particle size distribution of both iron and hematite powders. The average size of Fe_2O_3 was estimated at 0.5 and 0.7 µm, respectively (for 10 and 20 sol. %, see Figure A1). Small growth of mean particle size proportionally to the temperature of reduction was observed (Figure 3 and Table 1). Reduction processes insignificantly increased the mean size of the particles at temperatures below 450 °C. The mass fraction of α-Fe increased when the reduction temperature increased, but high temperature led to the destruction of nanostructured spherical particles to smaller particles of which the former was composed. For iron powder (10 sol. %), spheres broke down at 500 °C (Figure 2d). For another sample (20 sol. %), similar destruction presumably can be obtained at higher temperatures than 500 °C.

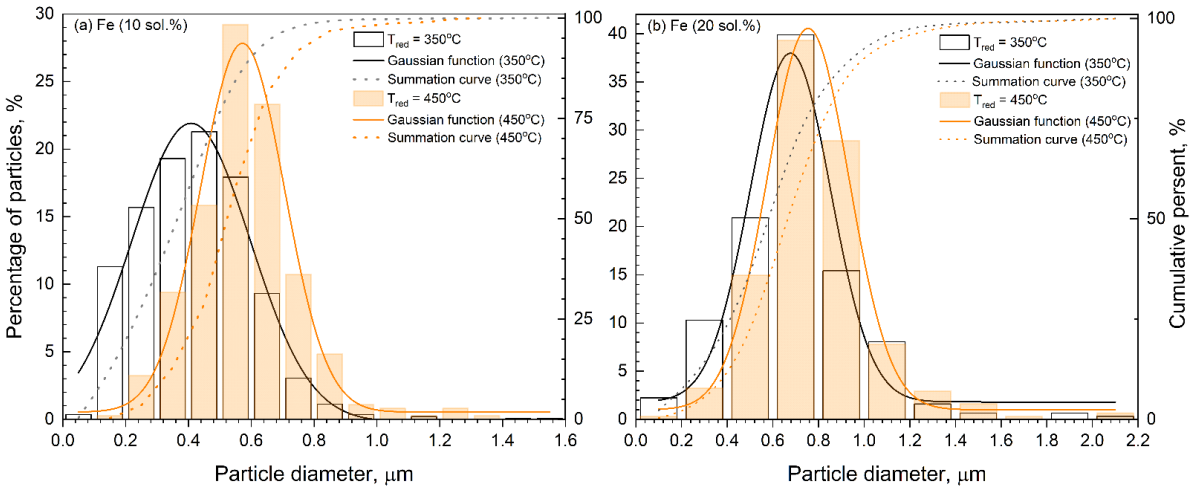

Figure 3. Particle size distribution of iron powders (**a**) Fe 10 sol. % and (**b**) 20 sol. % produced at 350 and 450 °C reduction temperatures.

3.3. Thermal Analysis

Simultaneous (TG-DSC) thermal analysis was performed for all obtained iron powders (Table 2). In the TG-DSC analysis of the samples "500 °C" the presence of exothermic reaction between iron powder and oxidizer in the range from 100 to 570 °C was observed (Figure 4). The value of the oxidized iron powder mass gain was the closest to the theoretical value, calculated from the chemical reaction, which was 42.97%. That indicated iron powder purity and can be compared with quantitative X-ray diffraction results (see Table 1).

Table 2. The simultaneous thermal analysis data of measurements of the iron powders, where T_{onset}—onset temperature of oxidization; ΔH—total heat generation; Δm—total mass gain at 999 °C; ω^{Fe}—fraction of iron estimated using STA results.

Sample	T_{red}, °C	T_{onset}, °C	ΔH, J/g	Δm, %	ω^{Fe}, %
Fe (10 sol. %)	350	128.2	6227	33.64	78
	400	104.5	5660	35.12	82
	450	165.0	5369	32.01	74
	500	144.8	7285	38.04	89
Fe (20 sol. %)	350	118.1	5850	35.56	83
	400	128.3	6120	37.62	88
	450	135.8	5820	36.09	84
	500	136.0	6570	38.64	90

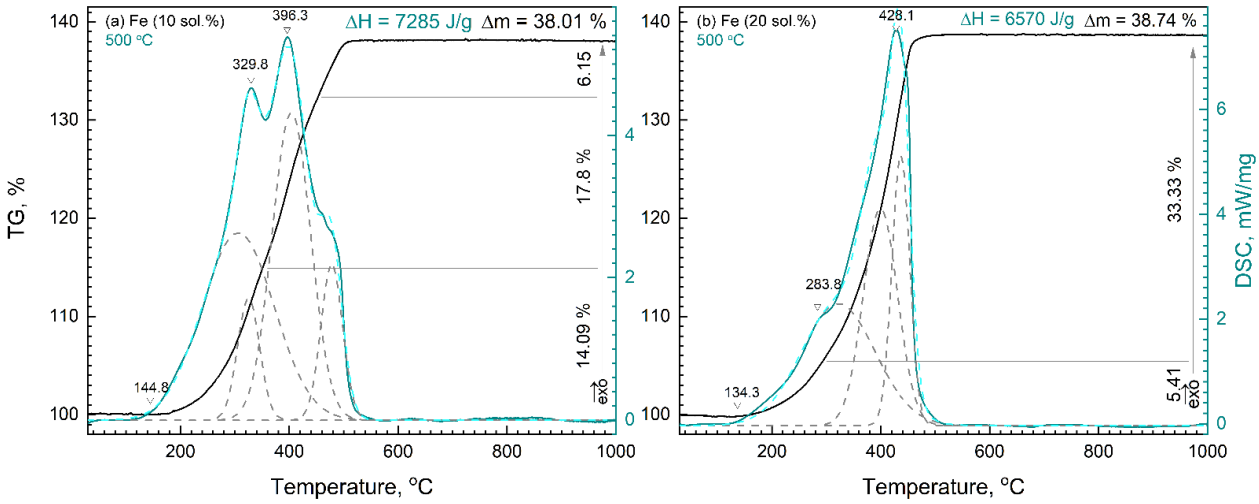

Figure 4. Simultaneous thermal analysis of Fe (**a**) 10 sol. % and (**b**) 20 sol. %, reduced at 500 °C in hydrogen. Dashed lines indicate the deconvolution of the peaks.

The thermal effects started above 100 °C and finished at 600 °C. The onset temperature shifted to higher temperatures with an increase in the reduction temperature. In Figure 4, both samples demonstrate two exothermic reaction peaks, which is typical for other powders. The total heat released, derived from the area under the curve, was 7.285 and 6.570 kJ·g^{-1} for samples 10 and 20 sol. %, respectively, reduced at 500 °C. Weak deviations in size [36], surface area, and porosity of particles as well as in grains and crystallinity [37] caused a variability of the values of onset temperature, the total released energy, and the mass gain.

As can be observed in Figure 4, the mass gain occurred in two stages. The deconvolution of the DSC-peaks is related to iron oxidation steps in the following order of reactions: Fe → (FeO) → Fe_3O_4 → Fe_2O_3 [38]. The oxidation of iron at the first stage can be described with the parallel production of magnetite Fe_3O_4 and hematite Fe_2O_3. Then, in the second stage, residual Fe_3O_4 is oxidized to Fe_2O_3 [36]. Three of the four deconvoluted peaks may be described with these reactions. The fourth peak, observed at temperatures above 570 °C [39] (*vide* Figure 4a), may be related to the wüstite formation. The correlation of the fitting curves obtained by deconvolution was greater than 0.99.

Considering STA, XRD, and SEM results, the 400 °C temperature is the optimum for annealing hematite powder in a hydrogen atmosphere to produce the chemically pure (~90%) iron powder with a sleek surface of particles, low porosity and large crystallite size (36–37 nm). The chemical purity of a metal is essential for its magnetic properties.

3.4. Microwave Measurement

The measured frequency dependencies of microwave permittivity and permeability are illustrated in Figures 5 and 6. The composites demonstrated intense microwave absorption. The imaginary permeability of the composite filled with the most chemically pure powder (T_{red} = 500 °C) exhibited almost as high maximum amplitude as that of carbonyl iron [4], which is usually considered a "standard" commercially available form of pure iron powder (see Figure 6, curve "66 and 81 wt. %"). The ferromagnetic resonance frequency (FMR), which is the frequency where the real permeability equals unity, was approximately 20 GHz for all studied composites. The imaginary permeability exhibited two magnetic loss peaks: the low-frequency (LF) peak, located at 0.3–2 GHz, depending on sample properties, and the high-frequency (HF) peak, at around 8–11 GHz. Precise peak positions as well as Acher's parameters are given in Table 3. Both LF and HF peak positions were found to depend on the chemical purity of iron but not on the size of the particles (see Table 3: peak positions for each temperature were almost the same between samples). The LF peak was also found to be of higher relative amplitude for particles of Fe 10 sol. % sample than that

of particles of Fe 20 sol. %. The low-frequency maximum in the imaginary permeability curve is usually deemed to be attributed to the effect of eddy currents [2], and the motion of domain walls [26,40]. In this case, the LF peak position is too high to be dealt with a domain wall motion. The physical origins of this absorption peak require further study. The HF maximum was related to the natural ferromagnetic resonance [4].

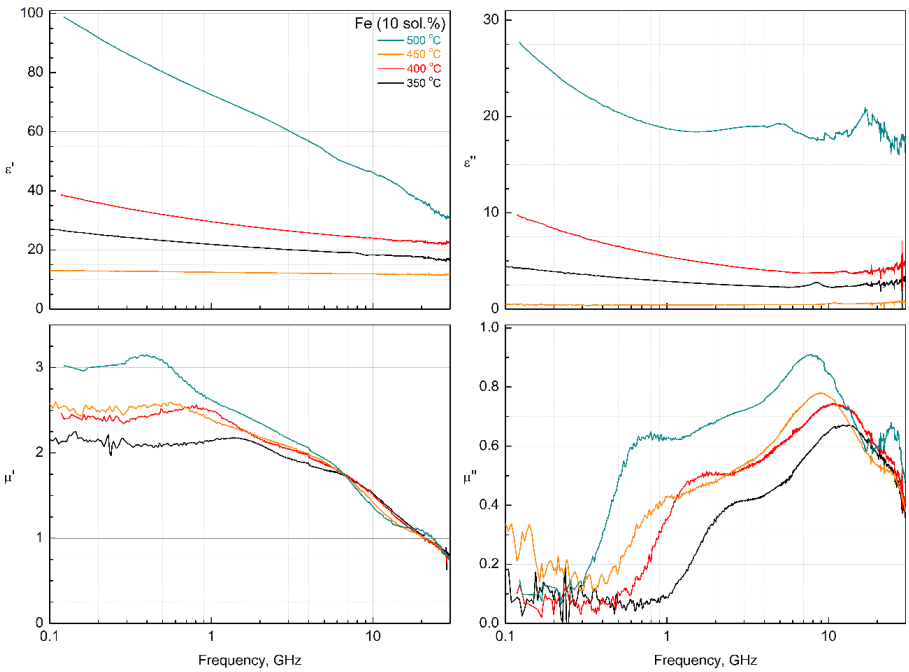

Figure 5. The frequency dependences of complex microwave characteristics of the wax-based composites filled with 75 wt. % (25 vol. %) fraction of Fe (10 sol. %) powder.

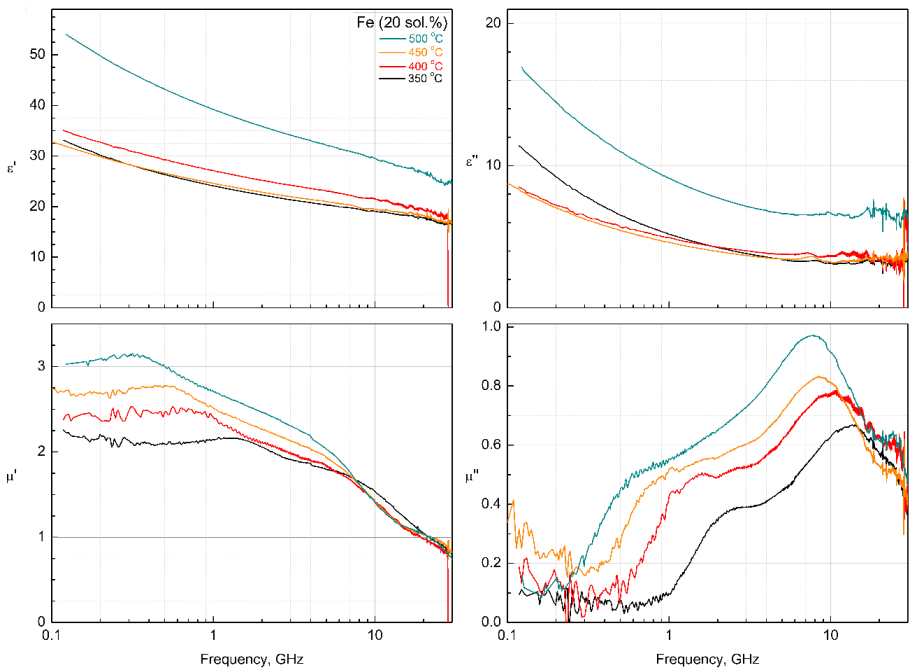

Figure 6. The frequency dependencies of complex microwave characteristics of the wax-based composites filled with 75 wt. % (25 vol. %) fraction of Fe (20 sol. %) powder.

Table 3. Dynamic magnetic characteristics of the wax-based composites filled Fe powders under study, where K_A—the Acher's parameter; f_{LF} and f_{HF}—position of low and high-frequency peaks; ρ_{incl}—density of iron powder inclusions in wax-based composites.

Sample	T_{red}, °C	K_A	f_{LF}, GHz	f_{HF}, GHz	ρ_{incl}, g/cm^3
Fe (*10 sol. %*)	350	0.176	2.4	13.9	6.17
	400	0.192	1.6	10.6	5.91
	450	0.178	1.0	8.5	6.10
	500	0.210	0.7	7.7	6.64
Fe (*20 sol. %*)	350	0.177	2.5	13.1	6.04
	400	0.184	1.7	11.0	6.37
	450	0.185	1.0	9.0	6.18
	500	0.212	0.8	7.9	6.55

An increase in the temperature of hydrogen reduction led to an increase in the amplitude and a decrease in the resonance frequency (damping maxima) for both LF and HF peaks in all cases. The correlation observed was: (a) the higher the chemical purity of α-Fe had been; and (b) the lower had been the measured damping maxima. Smaller (10 sol %) particles of pure α-Fe showed an LF peak of a higher quality factor than larger particles (20 sol %).

In addition to these changes, there is a qualitative distinction between "350 °C" and "400 °C" vs. "450 °C" and "500 °C" samples. An increase in temperature higher than 400 °C by treatment with hydrogen decreased the Q-factor of the ferromagnetic resonance peak and decreased magnetic losses above ~15 GHz. Therefore, 400 °C is the threshold temperature that qualitatively changes the microwave permeability of these powders. Two phenomena contribute to these changes: an increase in the chemical purity of the iron powder and a decrease in effective particle size caused by the partial destruction of the spheres, which was observed in Figure 2. Comparing properties of spherical powders of the same size but different chemical purity of α-Fe, it was observed that chemical composition significantly affects microwave permeability. This result adds substantial information to the knowledge that allows dynamic magnetic properties to fine-tune the desired composite materials.

The calculated integral Acher's parameter was within the range of 0.170 to 0.215, which was typical for spherical particles of carbonyl iron. A monotonic increase in K_A value with the increase in temperature of reduction (except the "400 °C" samples of both samples) correlates well with the increase in a fraction of α-Fe determined using both XRD and STA techniques. This may be interpreted as an increase in the effective volume of pure iron in the sample. The "400 °C" samples showed high Acher's parameter which indicates high efficiency in microwave absorption among other samples.

The high permittivity for the composite filled with the most chemically pure iron is attributed to the destruction of initial spherical particles which is especially noticeable in Figure 2. The presence of not only spherical particles of ~1-micron size but rather 0.1–1 size distribution noticeably affected the permittivity value.

4. Conclusions

Ferromagnetic nanostructured iron powders were obtained using a two-stage process involving spray-pyrolysis and reduction in hydrogen. The powders were obtained from iron nitrate aqueous solution (10 and 20 wt. %). In the first stage, the hematite powders with a mean diameter of 0.5 and 0.7 μm were synthesized, respectively, to the concentration of initial solutions. In the second stage, iron powders were obtained from hematite in hydrogen flow. The reduction process was carried out at 350, 400, 450, and 500 °C. The reduction of two iron oxide powders, 0.5 and 0.7 μm in diameter, at given temperatures, resulted in eight sample types to study in total.

It was found that the temperature reduction influenced grain size, crystallite size, porosity, and chemical purity of the product. As the reduction developed, iron oxide

loses weight and volume, and then the newly formed a-Fe crystalizes. These processes resulted in particles essentially of the same size as initial iron oxide, but of porous, mesh structure, consisting of iron grains. The threshold temperature of reduction that gave distinct porous iron particles was found to be 400 °C. Reduction at 500 °C caused even higher grain growth, which led to partial destruction of the initially spherical particles. XRD showed the presence of α-Fe and α-Fe_2O_3 phases in all samples. The a-Fe phase purity was estimated to be 85 mass. % when reduced at 350 °C, and 95 mass. % when reduced at 500 °C. Thermogravimetric data coincided well with the XRD measurements.

Variations in the reduction temperature significantly affected microwave permeability. It is important to note that the reduction temperature did not change the shape and size of the particles, which are well known to govern microwave permeability and permittivity. An increase in the chemical purity of iron particles increased the value of Acher's parameter, which is the quantitative characteristic of the dynamic magnetic performance of a material. Additionally, an increase in the chemical purity of iron increased the amplitude of both the real and imaginary parts of the permeability and shifted magnetic loss peaks to lower frequencies. Among other samples, powders obtained at 400 °C demonstrated distinct characteristics. Those possessed simultaneously high chemical purity, low porosity, high Acher's parameter, and high magnetic losses at around 15 GHz frequency range.

The results obtained enhance our understanding of the relationship between the chemical conditions of iron and the dynamic magnetic properties of iron-based composite materials.

Author Contributions: Conceptualization, A.V.A. and S.S.M.; methodology, A.V.A., S.S.M., A.O.S. and D.A.P.; software, A.V.A., A.O.S. and D.A.P.; validation, A.V.A., S.S.M. and A.V.O.; formal analysis, A.V.A., S.S.M., A.O.S., A.V.O., D.A.P., K.N.R. and A.N.L.; investigation, A.V.A. and A.O.S.; resources, A.V.A. and S.S.M.; data curation, A.V.A., A.O.S., A.V.O. and D.A.P.; writing—original draft preparation, A.V.A.; writing—review and editing, A.V.A., S.S.M., A.O.S., A.V.O., D.A.P. and K.N.R.; visualization, A.V.A. and S.S.M.; supervision, S.S.M., K.N.R. and A.N.L.; project administration, S.S.M. and A.N.L.; funding acquisition, S.S.M. and A.N.L. All authors have read and agreed to the published version of the manuscript.

Funding: This research was funded by the Russian Science Foundation (RSF), grant number 21-19-00138 (https://rscf.ru/en/project/21-19-00138/, accessed on 1 January 2023).

Data Availability Statement: Data are contained within the article.

Conflicts of Interest: The authors declare no conflict of interest. The funders had no role in the design of the study; in the collection, analyses, or interpretation of data; in the writing of the manuscript, or in the decision to publish the results.

Appendix A

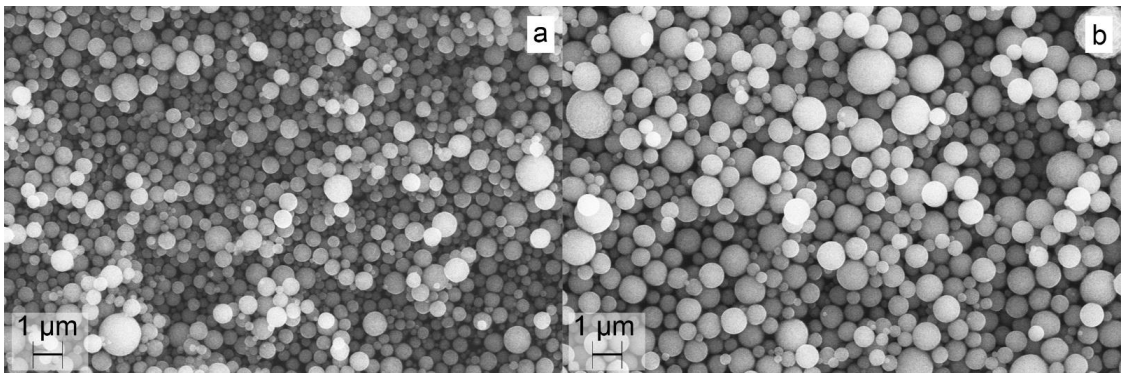

Figure A1. SEM images of the (**a**) 10 sol. % and (**b**) 20 sol. % hematite Fe_2O_3 powders produced at 1000 °C.

References

1. Acher, O. Frequency Response Engineering of Magnetic Composite Materials. In *Advances in Electromagnetics of Complex Media and Metamaterials*; Springer: Dordrecht, The Netherlands, 2002; pp. 39–59.
2. Rozanov, K.N.; Koledintseva, M.Y. Application of Generalized Snoek's Law over a Finite Frequency Range: A Case Study. *J. Appl. Phys.* **2016**, *119*, 073901. [CrossRef]
3. Dolmatov, A.V.; Maklakov, S.S.; Zezyulina, P.A.; Osipov, A.V.; Petrov, D.A.; Naboko, A.S.; Polozov, V.I.; Maklakov, S.A.; Starostenko, S.N.; Lagarkov, A.N. Deposition of a Sio2 Shell of Variable Thickness and Chemical Composition to Carbonyl Iron: Synthesis and Microwave Measurements. *Sensors* **2021**, *21*, 4624. [CrossRef] [PubMed]
4. Maklakov, S.S.; Lagarkov, A.N.; Maklakov, S.A.; Adamovich, Y.A.; Petrov, D.A.; Rozanov, K.N.; Ryzhikov, I.A.; Zarubina, A.Y.; Pokholok, K.V.; Filimonov, D.S. Corrosion-Resistive Magnetic Powder Fe@SiO 2 for Microwave Applications. *J. Alloys Compd.* **2017**, *706*, 267–273. [CrossRef]
5. Abbas, S.M.; Dixit, A.K.; Chatterjee, R.; Goel, T.C. Complex Permittivity, Complex Permeability and Microwave Absorption Properties of Ferrite–Polymer Composites. *J. Magn. Magn. Mater.* **2007**, *309*, 20–24. [CrossRef]
6. Lagarkov, A.N.; Rozanov, K.N. High-Frequency Behavior of Magnetic Composites. *J. Magn. Magn. Mater.* **2009**, *321*, 2082–2092. [CrossRef]
7. Lv, Q.; Zhu, S.; Zhao, X.; Liu, X.; Feng, S.; Kan, X.; Yujie, Y.; Cheng, Y. Magnetic Permeability Stability of Composite Material with Nominal Composition Ni0.6Fe2.4O4. *J. Magn. Magn. Mater.* **2022**, *553*, 169179. [CrossRef]
8. Battle, P.D.; Grandjean, F.; Long, G.J.; Oldham, S.E. The Influence of Chemical Composition on the Magnetic Properties of Fe1.5–XCoxRh0.5Mo3N ($0 \leq x \leq 1.5$). *J. Mater. Chem.* **2007**, *17*, 4785. [CrossRef]
9. Zezyulina, P.A.; Petrov, D.A.; Rozanov, K.N.; Vinnik, D.A.; Maklakov, S.S.; Zhivulin, V.E.; Starikov, A.Y.; Sherstyuk, D.P.; Shannigrahi, S. Study of the Static and Microwave Magnetic Properties of Nanostructured BaFe12−xTixO19. *Coatings* **2020**, *10*, 789. [CrossRef]
10. Maklakov, S.S.; Naboko, A.S.; Maklakov, S.A.; Bobrovskii, S.Y.; Polozov, V.I.; Zezyulina, P.A.; Osipov, A.V.; Ryzhikov, I.A.; Rozanov, K.N.; Filimonov, D.F.; et al. Amorphization of Thin Supermalloy Films Ni79Fe17Mo4 with Oxygen during Magnetron Sputtering. *J. Alloys Compd.* **2021**, *854*, 157097. [CrossRef]
11. Howlader, R.K.; Shil, S.K.; Shekher Sikder, S.; Kumar Saha, D. Effect of Annealing Temperature on the Complex Permeability of (Fe0.95Co0.05)73.5Cu1Nb3Si13.5B9 Nanocrystalline Amorphous Ribbon. *Res. Rev. J. Mater. Sci.* **2017**, *05*, 144–148. [CrossRef]
12. Sanna Angotzi, M.; Mameli, V.; Zákutná, D.; Kubániová, D.; Cara, C.; Cannas, C. Evolution of the Magnetic and Structural Properties with the Chemical Composition in Oleate-Capped Mn(x)Co(1–x)Fe2O4 Nanoparticles. *J. Phys. Chem. C* **2021**, *125*, 20626–20638. [CrossRef]
13. Yudin, A.; Shatrova, N.; Khaydarov, B.; Kuznetsov, D.; Dzidziguri, E.; Issi, J.-P. Synthesis of Hollow Nanostructured Nickel Oxide Microspheres by Ultrasonic Spray Atomization. *J. Aerosol Sci.* **2016**, *98*, 30–40. [CrossRef]
14. Nandiyanto, A.B.D.; Okuyama, K. Progress in Developing Spray-Drying Methods for the Production of Controlled Morphology Particles: From the Nanometer to Submicrometer Size Ranges. *Adv. Powder Technol.* **2011**, *22*, 1–19. [CrossRef]
15. Gurmen, S.; Ebin, B.; Stopić, S.; Friedrich, B. Nanocrystalline Spherical Iron–Nickel (Fe–Ni) Alloy Particles Prepared by Ultrasonic Spray Pyrolysis and Hydrogen Reduction (USP-HR). *J. Alloys Compd.* **2009**, *480*, 529–533. [CrossRef]
16. Septiani, E.L.; Kikkawa, J.; Cao, K.L.A.; Hirano, T.; Okuda, N.; Matsumoto, H.; Enokido, Y.; Ogi, T. Direct Synthesis of Submicron FeNi Particles via Spray Pyrolysis Using Various Reduction Agents. *Adv. Powder Technol.* **2021**, *32*, 4263–4272. [CrossRef]
17. Halim, K.S.A.; El-Geassy, A.A.; Ramadan, M.; Nasr, M.I.; Hussein, A.; Fathy, N.; Alghamdi, A.S. Reduction Behavior and Characteristics of Metal Oxides in the Nanoscale. *Metals* **2022**, *12*, 2182. [CrossRef]
18. Gorimbo, J.; Muvhiiwa, R.; Llane, E.; Hildebrandt, D. Cobalt Catalyst Reduction Thermodynamics in Fischer Tropsch: An Attainable Region Approach. *Reactions* **2020**, *1*, 115–129. [CrossRef]
19. Kosevich, A.; Petrusevich, E.; Maklakov, S.; Naboko, A.; Kolesnikov, E.; Petrov, D.; Zezyulina, P.; Pokholok, K.; Filimonov, D.; Han, M. Low Weight Hollow Microspheres of Iron with Thin Dielectric Coating: Synthesis and Microwave Permeability. *Coatings* **2020**, *10*, 995. [CrossRef]
20. Artemova, A.V.; Maklakov, S.S.; Osipov, A.V.; Petrov, D.A.; Shiryaev, A.O.; Rozanov, K.N.; Lagarkov, A.N. The Size Dependence of Microwave Permeability of Hollow Iron Particles. *Sensors* **2022**, *22*, 3086. [CrossRef]
21. Konyukhov, Y.V.; Kamali, S.; Nguyen, T.H.; Alymov, M.I.; Lileev, A.S.; Karpenkov, D.Y.; Zakharova, E.V. Size Dependence of Magnetic Properties of Fe, Co and Ni Nanoparticles Prepared by the Chemical-Metallurgical Method Using Surfactants. *Nano-Struct. Nano-Objects* **2023**, *33*, 100943. [CrossRef]
22. Dolmatov, A.V.; Maklakov, S.S.; Artemova, A.V.; Petrov, D.A.; Shiryaev, A.O.; Lagarkov, A.N. Deposition of Thick SiO2 Coatings to Carbonyl Iron Microparticles for Thermal Stability and Microwave Performance. *Sensors* **2023**, *23*, 1727. [CrossRef] [PubMed]
23. Shiryaev, A.; Rozanov, K.; Naboko, A.; Artemova, A.; Maklakov, S.; Bobrovskii, S.; Petrov, D. Splitting of the Magnetic Loss Peak of Composites under External Magnetic Field. *Physics* **2021**, *3*, 678–688. [CrossRef]
24. Starostenko, S.N.; Petrov, D.A.; Shiryaev, A.O. Effect of Temperature on Microwave Permeability Spectrum of Composite with Gadolinium Powder. *Mod. Electrodyn.* **2022**, *2*, 23–31.
25. Starostenko, S.N.; Petrov, D.A.; Rozanov, K.N.; Shiryaev, A.O.; Lomaeva, S.F. Effect of Temperature on Microwave Permeability of an Air-Stable Composite Filled with Gadolinium Powder. *Sensors* **2022**, *22*, 3005. [CrossRef]

26. Nakamura, T. Snoek's Limit in High-Frequency Permeability of Polycrystalline Ni–Zn, Mg–Zn, and Ni–Zn–Cu Spinel Ferrites. *J. Appl. Phys.* **2000**, *88*, 348–353. [CrossRef]
27. Iakubov, I.T.; Lagarkov, A.N.; Maklakov, S.A.; Osipov, A.V.; Rozanov, K.N.; Ryzhikov, I.A.; Starostenko, S.N. Microwave Permeability of Composites Filled with Thin Fe Films. *J. Magn. Magn. Mater.* **2006**, *300*, e74–e77. [CrossRef]
28. Lagarkov, A.N.; Rozanov, K.N.; Simonov, N.A.; Starostenko, S.N. Microwave Permeability of Magnetic Films. In *Handbook of Advanced Magnetic Materials*; Springer: Boston, MA, USA, 2006; pp. 1742–1773.
29. Petrov, D.A.; Rozanov, K.N.; Koledintseva, M.Y. Influence of Higher-Order Modes in Coaxial Waveguide on Measurements of Material Parameters. In Proceedings of the 2018 IEEE Symposium on Electromagnetic Compatibility, Signal Integrity and Power Integrity (EMC, SI & PI), Long Beach, CA, USA, 30 July–3 August 2018; IEEE: New York, NY, USA, 2018; pp. 66–70.
30. Kraushofer, F.; Jakub, Z.; Bichler, M.; Hulva, J.; Drmota, P.; Weinold, M.; Schmid, M.; Setvin, M.; Diebold, U.; Blaha, P.; et al. Atomic-Scale Structure of the Hematite α-Fe_2O_3 (1102) "R-Cut" Surface. *J. Phys. Chem. C* **2018**, *122*, 1657–1669. [CrossRef]
31. Bak, S.-M.; Shadike, Z.; Lin, R.; Yu, X.; Yang, X.-Q. In Situ/Operando Synchrotron-Based X-Ray Techniques for Lithium-Ion Battery Research. *NPG Asia Mater.* **2018**, *10*, 563–580. [CrossRef]
32. Pang, J.; Guo, P.; Zhao, P. Reduction Kinetics of Fine Iron Ore Powder in Mixtures of H2-N2 and H2-H2O-N2 of Fluidized Bed. *J. Iron Steel Res. Int.* **2015**, *22*, 391–395. [CrossRef]
33. El-geassy, A.A.; El-kashif, F.O.; Nasr, M.I.; Omar, A.A. Kinetics and Mechanisms of Com Pacts Re-Oxiation of Freshly Reduced Lron. *ISIJ Int.* **1994**, *34*, 541–547. [CrossRef]
34. Beach, G.S.D.; Parker, F.T.; Smith, D.J.; Crozier, P.A.; Berkowitz, A.E. New Magnetic Order in Buried Native Iron Oxide Layers. *Phys. Rev. Lett.* **2003**, *91*, 267201. [CrossRef] [PubMed]
35. Shatrova, N.; Yudin, A.; Levina, V.; Kuznetsov, D.; Novakova, A.; Dzidziguri, E.; Perov, N.; Issi, J.-P. Characteristics of Co3O4 and Cobalt Nanostructured Microspheres: Morphology, Structure, Reduction Process, and Magnetic Properties. *Mater. Res. Bull.* **2018**, *99*, 189–195. [CrossRef]
36. Lysenko, E.N.; Surzhikov, A.P.; Zhuravkov, S.P.; Vlasov, V.A.; Pustovalov, A.v.; Yavorovsky, N.A. The Oxidation Kinetics Study of Ultrafine Iron Powders by Thermogravimetric Analysis. *J. Therm. Anal. Calorim.* **2014**, *115*, 1447–1452. [CrossRef]
37. Müller, C.M.O.; Pires, A.T.N.; Yamashita, F. Characterization of Thermoplastic Starch/Poly(Lactic Acid) Blends Obtained by Extrusion and Thermopressing. *J. Braz. Chem. Soc.* **2012**, *23*, 426–434. [CrossRef]
38. Chen, R.Y.; Yeun, W.Y.D. Review of the High-Temperature Oxidation of Iron and Carbon Steels in Air or Oxygen. *Oxid. Met.* **2003**, *59*, 433–468. [CrossRef]
39. Spreitzer, D.; Schenk, J. Reduction of Iron Oxides with Hydrogen—A Review. *Steel Res. Int.* **2019**, *90*, 1900108. [CrossRef]
40. Shiryaev, A.O.; Rozanov, K.N.; Artemova, A.V.; Bobrovskii, S.Y.; Naboko, A.S.; Osipov, A.V.; Petrov, D.A.; Zezyulina, P.A. Experimental Study Of Microwave Magnetic Properties Of Composites Under Magnetic Bias. In Proceedings of the 2021 IEEE International Magnetic Conference (INTERMAG), Lyon, France, 26–30 April 2021; IEEE: New York, NY, USA, 2021; pp. 1–5.